Combined spin orientation and phase function of asteroids

B. Carry, J. Peloton, R. Le Montagner, M. Mahlke, J. Berthier

A&A, 687, A38 (2024)
https://doi.org/10.1051/0004-6361/202449789

Astronomy & Astrophysics

Combined spin orientation and phase function of asteroids⋆

B. Carry[1], J. Peloton[2], R. Le Montagner[2], M. Mahlke[3], and J. Berthier[4]

[1] Université Côte d'Azur, Observatoire de la Côte d'Azur, CNRS, Laboratoire Lagrange, Nice, France
e-mail: benoit.carry@oca.eu
[2] Université Paris-Saclay, CNRS/IN2P3, IJCLab, 91405 Orsay, France
[3] Institut d'Astrophysique Spatiale, Université Paris-Saclay, CNRS, 91405 Orsay, France
[4] IMCCE, Observatoire de Paris, PSL Research University, CNRS, Sorbonne Universités, UPMC Univ Paris 06, Univ. Lille, Paris, France

Received 29 February 2024 / Accepted 4 April 2024

ABSTRACT

Context. Large sky surveys provide numerous non-targeted observations of small bodies of the Solar System. The upcoming LSST of the *Vera C. Rubin* Observatory will be the largest source of small body photometry in the next decade. With non-coordinated epochs of observation, colors – and therefore taxonomy and composition – can only be computed by comparing absolute magnitudes obtained in each filter by solving the phase function (evolution of brightness of the small body against the solar phase angle). Current models in use in the community (HG, $HG^{\star}_{12}$, and HG_1G_2), however, fail to reproduce the long-term photometry of many targets due to the change in the aspect angle between apparitions.

Aims. We aim to derive a generic yet simple phase function model accounting for the variable geometry of the small bodies over multiple apparitions.

Methods. As a spinoff of the HG_1G_2 model, we propose the sHG_1G_2 phase function model in which we introduce a term describing the brightness changes due to spin orientation and polar oblateness. We applied this new model to 13 245 908 observations of 122 675 Solar System objects (SSOs). These observations were acquired in the *g* and *r* filters with the Zwicky Transient Facility between November 1, 2019 and December 1, 2023. We retrieved them and implemented the new sHG_1G_2 model in FINK, a broker of alerts designed for the LSST.

Results. The sHG_1G_2 model leads to smaller residuals than other phase function models, providing a better description of the photometry of asteroids. We determined the absolute magnitude, *H*, and phase function coefficients (G_1, G_2) in each filter, the spin orientation (α_0, δ_0), and the polar-to-equatorial oblateness, *R*, for 95 593 SSOs, which constitutes about a tenfold increase in the number of characterized objects compared to the current census.

Conclusions. The application of the sHG_1G_2 model to ZTF alert data using the FINK broker shows that the model is appropriate for extracting physical properties of asteroids from multi-band and sparse photometry, such as the forthcoming LSST survey.

Key words. methods: data analysis – techniques: photometric – minor planets, asteroids: general

1. Introduction

Called vermin of the sky by astronomers for a long time owing to the trails they left on photographic plates (Seares 1930), the accidental observations of asteroids in large sky surveys have seen a growing interest. While the cadence and mode of operation of most surveys are seldom optimized for moving objects (Solano et al. 2014), the tremendous amount of data acquired in modern times can provide a wealth of information on the compositional and physical properties of Solar System objects (SSOs), unattainable by dedicated observations and yet crucial to deciphering the events that sculpted our Solar System.

Spectrophotometry is required to determine the taxonomy (DeMeo & Carry 2013; Popescu et al. 2018), and hence composition, of objects and to map their distribution, relics of the timing, and place of formation, together with past dynamical events (DeMeo & Carry 2014). Photometry time series are necessary to determine the rotation period and spin coordinates (Kaasalainen et al. 2001; Kaasalainen 2004), which are critical parameters dictating the dynamical evolution of asteroids through the Yarkovsky effect (Farinella et al. 1998; Vokrouhlický et al. 2015), spreading dynamical structures over time (Bottke et al. 2001; Vokrouhlický et al. 2006).

Decades of targeted observations (e.g., Zellner et al. 1985; Xu et al. 1995; Bus & Binzel 2002; Lazzaro et al. 2004; DeMeo et al. 2014; Lucas et al. 2017; Devogèle et al. 2018; De Prá et al. 2018; Binzel et al. 2019) have, however, brought about 7 000 visible and near-infrared spectra only (see the compilation in the Mahlke et al. (2022) taxonomy). The situation is even more dramatic for physical properties, focusing here on rotation period and spin-axis coordinates. Detailed studies using stellar occultations, disk-resolved imaging, or radar echoes have characterized only a few tens of SSOs (e.g., Veverka et al. 2000; Ostro et al. 2006; Carry et al. 2010; Sierks et al. 2011; Tanga et al. 2015; Pajuelo et al. 2018; Vernazza et al. 2021). The most-productive method has been light curve inversion, mainly using the inversion algorithm of Kaasalainen et al. (2001). However, decades of patient accumulation of light curves only brought solutions for a few hundred SSOs (Kaasalainen et al. 2002; Torppa et al. 2003; Slivan et al. 2003; Ďurech et al. 2007).

⋆ The data presented here are available at the CDS via anonymous ftp to cdsarc.cds.unistra.fr (130.79.128.5) or via https://cdsarc.cds.unistra.fr/viz-bin/cat/J/A+A/687/A38

The game changer has been the data mining of serendipitous observations of SSOs in large sky surveys, through dedicated software. The Sloan Digital Sky Survey (SDSS), the ESO VISTA Hemispherical Survey (VHS), and the SkyMapper Southern Survey (SMSS) have brought hundreds of thousands of multi-filter photometric observations of asteroids (e.g., Ivezić et al. 2001; Carry et al. 2016; Popescu et al. 2016; Sergeyev et al. 2022), resulting in the determination of the taxonomic class of about 143 000 SSOs (11% of the population, see the compilation in the SsODNet service[1], Berthier et al. 2023). The ESA *Gaia* mission released spectroscopy for over 60,000 asteroids (Galluccio et al. 2023; Oszkiewicz et al. 2023; Galinier et al. 2023). The Catalina Sky Survey, the Lowell Observatory database, NASA's *Kepler*/K2 and TESS, the Palomar Transient Factory (PTF), and ESA *Gaia* have brought a wealth of photometry on most targets (Hanuš et al. 2013b; Waszczak et al. 2015; Chang et al. 2015; Berthier et al. 2016; Ďurech et al. 2016, 2019; Ďurech & Hanuš 2023, 2018; Pál et al. 2020; Spoto et al. 2018; Muinonen et al. 2020; Kalup et al. 2021), albeit mainly sparse in time (i.e., the frequency of observations is much lower than the intrinsic rotation frequency). Most important is the theoretical framework to benefit from this photometry sparse in time (Kaasalainen 2004). Nevertheless, rotation periods are only available for about 33 000 asteroids (2.5% of the population) and spin coordinates for 10 000 (0.7%) only (see Berthier et al. 2023).

The upcoming LSST of the *Vera C. Rubin* Observatory is expected to discover around 5 million SSOs (LSST Collaboration 2009). The determination of their taxonomy and surface composition based on the provided observations is not simple. Owing to their irregular shape and constantly changing geometry, the photometry of SSOs is a degenerate combination of intrinsic color and geometry. The determination of their colors hence generally relies on photometry acquired over short timescales, typically within minutes (Popescu et al. 2016). While this condition is fulfilled by the modes of operation of the SDSS, SkyMapper, and the ESA *Euclid* mission (Carry 2018; Sergeyev & Carry 2021; Sergeyev et al. 2022), the LSST will provide sparse photometry only (Jones et al. 2009). The determination of the colors of SSOs must therefore rely on the determination of their absolute magnitude in each filter (Mahlke et al. 2021; Alvarez-Candal et al. 2022). It has been repeatedly shown, however, that the absolute magnitude and the slope of the phase function may vary from apparition to apparition (e.g., Kwiatkowski & Kryszczynska 1992; Carvano & Davalos 2015; Mahlke et al. 2021; Jackson et al. 2022). This severely increases the required number of observations per SSOs in a given apparition to determine its phase curve as observations from different apparitions cannot be combined as of today.

We introduce here a new model to benefit from the sparse photometry obtained over multiple bands from large sky surveys. We aim to provide a more accurate description of the photometry by simultaneously determining the absolute magnitude and phase coefficients in each band as well as the base geometric properties (spin coordinates and oblateness) of the SSOs. We describe this new model for multi-filter sparse photometry in Sect. 2. We present in Sect. 3 the data we used to validate the approach by comparing the new model with previous results from the community in Sect. 4. We present results for the asteroid phase function and spin orientation in Sect. 5. Finally, we provide easy and programmatic access to these results in Sect. 6.

2. Generalized model for sparse photometry

The absolute magnitude, H, of a SSO is defined as the magnitude of the object located at a heliocentric distance, Δ, of 1 au, a range to the observer, r, of 1 au, and a phase angle, γ, of 0°:

$$\begin{aligned} H &= H(r = 1, \Delta = 1, \gamma = 0) \\ &= m - f(r, \Delta) - g(\gamma), \end{aligned} \tag{1}$$

where

$$f(r, \Delta) = 5 \log_{10}(r\Delta) \tag{2}$$

$$\begin{aligned} g(\gamma) = -2.5 \log_{10} [&\mathtt{G}_1 \phi_1(\gamma) \\ &+ \mathtt{G}_2 \phi_2(\gamma) \\ &+ (1 - \mathtt{G}_1 - \mathtt{G}_2) \phi_3(\gamma)] , \end{aligned} \tag{3}$$

with the conditions

$$0 < \mathtt{G}_1, \tag{4a}$$

$$0 < \mathtt{G}_2, \tag{4b}$$

$$0 < 1 - \mathtt{G}_1 - \mathtt{G}_2, \tag{4c}$$

following the $\mathtt{HG}_1\mathtt{G}_2$ model of Muinonen et al. (2010), which was accepted in 2012 by the International Astronomical Union (IAU) as superseding the historical HG model (Bowell et al. 1989). The $\mathtt{HG}_1\mathtt{G}_2$ model offers a better description of the surge of brightness at low phase angles (called the opposition effect), and hence provides a more accurate determination of the absolute magnitude (Muinonen et al. 2010; Mahlke et al. 2021). Furthermore, the $\mathtt{G}_1\mathtt{G}_2$ parameters have been shown to be linked with albedo and taxonomic type (Shevchenko et al. 2016; Mahlke et al. 2021).

Although the $\mathtt{HG}_1\mathtt{G}_2$ model presents improvements over the HG model both in prediction and interpretation, its usage has remained limited so far. It has been used in a few studies, based mainly on targeted observations (Shevchenko et al. 2019, 2021, 2022) but also on sky surveys (in particular ESA *Gaia*, Martikainen et al. 2021; Colazo et al. 2021), including an extensive initial study by Oszkiewicz et al. (2011). However, ephemerides computation centers (Minor Planet Center[2], Jet Propulsion Laboratory Solar System Dynamics[3], and Lowell Observatory astorb[4]) report absolute magnitudes with the HG model and not $\mathtt{HG}_1\mathtt{G}_2$. Pragmatically, while HG always converges (especially as G is almost always fixed to the canonical value of 0.15), $\mathtt{HG}_1\mathtt{G}_2$ has strong requirements on phase coverage to produce meaningful results (in particular requiring observations at low phase angles, typically below 2–4°, see Mahlke et al. 2021). A two-parameter version of $\mathtt{HG}_1\mathtt{G}_2$ was proposed for that purpose by Muinonen et al. (2010) and refined by Penttilä et al. (2016), $\mathtt{HG}^{\star}_{12}$, although the absolute magnitudes derived with this latter model present systematic discrepancies with $\mathtt{HG}_1\mathtt{G}_2$ (Mahlke et al. 2021) due to the restricted parameter space.

However, the parameters of $\mathtt{HG}_1\mathtt{G}_2$ are wavelength-dependent. First, the absolute magnitude, H, is expected to be different for each observing band owing to the intrinsic color of the asteroid (close to Solar colors as a first approximation, see IMCCE 2021). This is already the case for the HG model,

[1] https://ssp.imcce.fr/webservices/ssodnet

[2] https://minorplanetcenter.net

[3] https://ssd.jpl.nasa.gov

[4] https://asteroid.lowell.edu/

in which H is implicitly H_V, the absolute magnitude reported in the Johnson V band[5]. The advantage of measuring the color based on absolute magnitudes is to avoid biases introduced by differences in observing time and brightness variation related to the shape of the SSO (Popescu et al. 2016; Carry 2018; Alvarez-Candal et al. 2022). Second, the G_1G_2 are also different (Mahlke et al. 2021), something which has been reported as "phase reddening" and observed spectrally in both laboratory samples and asteroids in the sky (Sanchez et al. 2012; Binzel et al. 2019; Alvarez-Candal 2024).

Furthermore, the HG_1G_2 model suffers from a major limitation: it does not account for the nonspherical geometry of asteroids (Jackson et al. 2022). Owing to the changing aspect angle (the angle between the spin axis and the viewing direction) over apparitions, the absolute magnitude can differ (see Fig. 10 in Mahlke et al. 2021, for instance). Conversely, a single HG or HG_1G_2 fit on a multi-opposition dataset will provide an average absolute magnitude but will likely result in biased magnitude predictions.

In the shape modeling formalism introduced by Kaasalainen et al. (2001), this aspect is solved by the simultaneous modeling of the 3D shape and the phase function (with a linear-exponential model). However, it typically requires more data (either dense light curves or many photometry measurements sparse in time) than for phase-function fitting only (see the discussion in Ďurech et al. 2015; Ďurech & Hanuš 2023).

We propose here an intermediate solution, dubbed sHG_1G_2 for $spinnedHG_1G_2$, solving the apparition-to-apparition change in magnitude without adding too many requirements to the dataset. It is in essence the "reference phase curve" defined by Kaasalainen et al. (2001). We introduced a new term, $s(\alpha, \delta)$, to the definition of the absolute magnitude, H (Eq. (2)), accounting for the orientation of the asteroid and function of its oblateness, R, and the equatorial coordinates of its spin axis (α_0, δ_0):

$$H = m - f(r, \Delta) - g(\gamma) - s(\alpha, \delta), \tag{5}$$

where

$$s(\alpha, \delta) = 2.5 \log_{10} \left[1 - (1 - R)|\cos \Lambda|\right], \tag{6}$$

with Λ the aspect angle, computed from the equatorial coordinates (α,δ) of the asteroid at the time of observation as

$$\cos \Lambda = \sin \delta \sin \delta_0 + \cos \delta \cos \delta_0 \cos (\alpha - \alpha_0). \tag{7}$$

Thus, an additional criterion was added to the definition of H: that it should correspond to the magnitude of the object at 1 au from both the Sun and the observer, with a 0° phase angle, seen from its equatorial plane As a corollary, the object is brighter by $2.5 \log_{10} R$ magnitudes when observed from its pole. Noting that $a > b > c$ the tri-axial diameters of the asteroid, R is the polar-to-equatorial oblateness ($0 < R \leq 1$):

$$R = \frac{c(a + b)}{2ab} \tag{8}$$

Applying this new definition of H to observations taken over several apparitions with different N_f filters, one can simultaneously determine the absolute magnitude, H, and phase parameters G_1G_2 for each band and the oblateness and spin coordinates for a total of $3 \times (N_f + 1)$ parameters. We present in Fig. 1 an illustration of the sHG_1G_2 model for the asteroid (22) Kalliope (we use the spin solution from Ferrais et al. 2022). The distance term, $f(r, \Delta)$, presents the expected minima and maxima at oppositions and conjunctions. The phase term, $g(\gamma)$, has a periodicity that is twice as fast, with a decreasing phase angle at both oppositions and conjunctions. Both are symmetric around epochs of a minimal phase angle (as is visible on the blue and orange curves). Their sum defines the HG_1G_2 model (Muinonen et al. 2010). The new term $s(\alpha, \delta)$ accounts for the slow change in geometry over time, allowing asymmetry. We present in Fig. 2 the phase and spin components ($g(\gamma)$ and $s(\alpha, \delta)$), similarly to Fig. 5 of Jackson et al. (2022). The phase curve is bounded between two extreme cases, the pole at ($\Lambda = \{0°, 180°\}$) and the equator at ($\Lambda = 90°$), and practically presents a slow evolution between these boundaries.

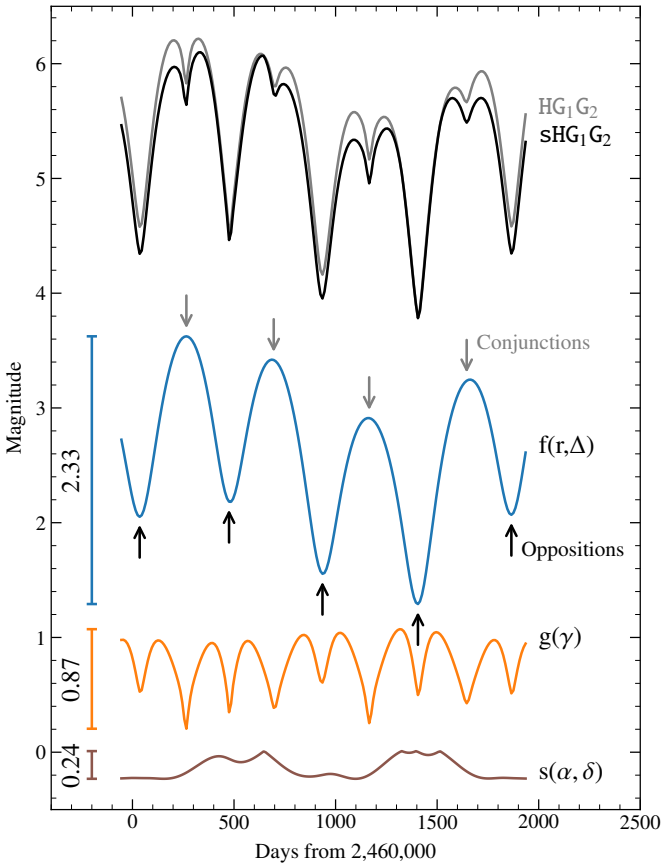

Fig. 1. sHG_1G_2 model of (22) Kalliope, with its three components – $f(r, \Delta)$, $g(\gamma)$, and $s(\alpha, \delta)$ – shown explicitly, together with their amplitude. The HG_1G_2 model is plotted for comparison.

3. Data

We implemented the sHG_1G_2 model in FINK[6], (Möller et al. 2021) a broker of alerts for the LSST (LSST Collaboration 2009). Today, before the start of the LSST, FINK processes daily the public stream of alerts from the Zwicky Transient Survey (ZTF; Masci et al. 2019; Graham et al. 2019; Bellm et al. 2019; Patterson et al. 2019).

[5] http://svo2.cab.inta-csic.es/theory/fps/index.php?id=Generic/Johnson.V (Rodrigo et al. 2012).

[6] https://fink-broker.org/

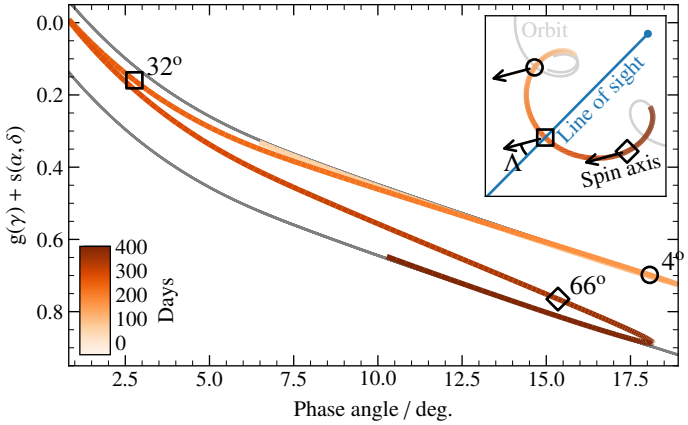

Fig. 2. Effect of the changing geometry (described by $s(\alpha, \delta)$) on the phase curve (traditionally $g(\gamma)$ only). Over 400 days from JD 2 460 000 (same as Fig. 1), (22) Kalliope is seen from an aspect angle increasing from 4° (pole on) to 78° (close to the equator) owing to motion as seen from the Earth. The inset presents the successive ecliptic (x,y) positions of Kalliope, color-coded by epoch, in a reference frame centered on Earth (the pale blue dot). Three reference epochs are drawn on both graphs (a circle, a square, and a diamond). The orientation of the spin axis of Kalliope is drawn as arrows at these three epochs, and the line of sight is drawn for the second (square) epoch, illustrating the aspect angle, Λ.

ZTF broadcasts a public stream for variable and transient events in two bands (g[7] and r[8], similar but not identical to the Sloan g and r filters, Bellm et al. 2019) of typically 215 000 alerts per night, of which about 70% is retained by FINK for scientific analyses, and 14% corresponds to SSOs. Between late 2019 and late 2023, FINK extracted 19 319 067 observations of SSOs from the ZTF public alert stream. FINK is one of the seven brokers of alerts being developed for the LSST. As such, the system has been designed to cope with a very large flow of data, covering all aspects of astrophysics, from the Solar System to variable stars, supernovae, and optical counterparts to gravitational wave events (e.g., Möller et al. 2021; Aivazyan et al. 2022; Leoni et al. 2022; Le Montagner et al. 2023). With the $\mathtt{sHG_1G_2}$ model implemented within FINK, its results are already freely available for each SSO through the FINK Web interface[9] and the corresponding Application Public Interface (API) SSO. We also propose a dedicated method to retrieve the parameters of the $\mathtt{sHG_1G_2}$ model for a large corpus of data at once: the Solar System Objects FINK Table[10] (SSOFT, see Sect. 6).

We used FINK to retrieve 19 319 067 observations of 565 045 unique SSOs in g and r between November 2019 and December 2023. We decided to only retain objects with at least 50 observations across all filter bands (122 675 unique SSOs). This threshold for the number of observations was chosen arbitrarily after several tests, as a compromise between the sample size and the fraction of objects failing to converge to a solution (see Sect. 4.1). The average number of observations (together with the 25% and 75% quantiles) is 92^{+46}_{-26}, for a length of observations (number of days between the first and the last observation) of $1,164^{+270}_{-108}$. We fit these observations with the HG (Bowell et al. 1989), $\mathtt{HG_1G_2}$ (Muinonen et al. 2010), and $\mathtt{sHG_1G_2}$ models, and compare the results in the following sections.

[7] http://svo2.cab.inta-csic.es/theory/fps/index.php?id=Palomar/ZTF.g
[8] http://svo2.cab.inta-csic.es/theory/fps/index.php?id=Palomar/ZTF.r
[9] https://fink-portal.org/
[10] https://fink-portal.org/api

4. Validation of the $\mathtt{sHG_1G_2}$ model

The improvement provided by $\mathtt{sHG_1G_2}$ is qualitatively visible in Fig. 3 for the asteroid (223) Rosa, a flyby candidate by the ESA JUICE mission (Grasset et al. 2013; Agostini et al. 2022). While the description of the opposition effect is different between HG and $\mathtt{HG_1G_2}$, they both predict a globally symmetric behavior around opposition. $\mathtt{sHG_1G_2}$ correctly describes the photometry as it accounts for the evolving geometry with time. We used the 122 675 SSOs to assert statistically the validity and limits of the $\mathtt{sHG_1G_2}$ model.

4.1. Success and failure

We imposed a set of boundaries for the parameters in the fitting process to guarantee meaningful results. Above all, we enforced that the conditions in Eqs. (4a) and (4b) be fulfilled, and that the oblateness, R, be between 0.3 and 1 (encompassing all published shape models; see Sect. 4.5).

Out of the 122 675 initial SSO light curves, the fitting procedure for the $\mathtt{sHG_1G_2}$ model converges in about 98% of cases. However, at this stage, there are suspicious solutions, where the minimization algorithm is clearly hitting the boundary conditions. Hence, in the following, we consider a solution to be fully valid if: the fitting procedure converges, the G_1 and G_2 values are non-singular (singular cases encompass values strictly equal to 0), the spin coordinates are non-singular (singular cases encompass α_0 strictly equal to 0° or 360°, (α_0,β_0) equals (180°,0°)), and the condition in Eq. (4c) is fulfilled (it could not be incorporated in the fitting procedure).

Using the two filter bands of ZTF (g and r), this results in a sample of 63 092 SSOs (51% success). This means about half of the fitted parameters are of good quality in all bands simultaneously (a similar success rate as Ďurech & Hanuš 2023, on *Gaia* photometry). As the phase parameters are fitted per band, we also defined the sample of SSOs for which the constraints on spin parameters defined above are fulfilled, and $\mathtt{G_1}$ and $\mathtt{G_2}$ fulfil the conditions in Eq. (4) for at least one filter band. This results in a sample of 95 593 SSOs (78% success). This sample will be used for the rest of the analysis unless explicitly stated.

For the HG model, the rate of success is higher, as was expected due to its simplistic form (98% success), but the $\mathtt{HG_1G_2}$ model has a somewhat lower success rate than the $\mathtt{sHG_1G_2}$ model (38% success in the two filter bands simultaneously, and 70% success in at least one filter band). This gives us confidence that the spin component in the light curve model contributes to ameliorating the parameter estimation globally compared to the $\mathtt{HG_1G_2}$ model.

Nonetheless, we have tried to understand the reasons for the failure of the $\mathtt{HG_1G_2}$ and $\mathtt{sHG_1G_2}$ models. The failures are not clearly correlated with the minimum phase angle, the number of observations per filter, the number of oppositions, and the range for the aspect angle values. Based on Fig. 1, we see that the contributions of the $g(\gamma)$ and $s(\alpha, \delta)$ components are relatively small compared to those of the other components, and often smaller than the typical error estimate on the photometric measurements reported in the ZTF alert packets. Hence, we might be in a noisy regime where the contributions from the phase and spin components are not always accessible. To test this hypothesis, we took the valid solutions for which the fitted procedure converges, and we randomized the magnitudes for each

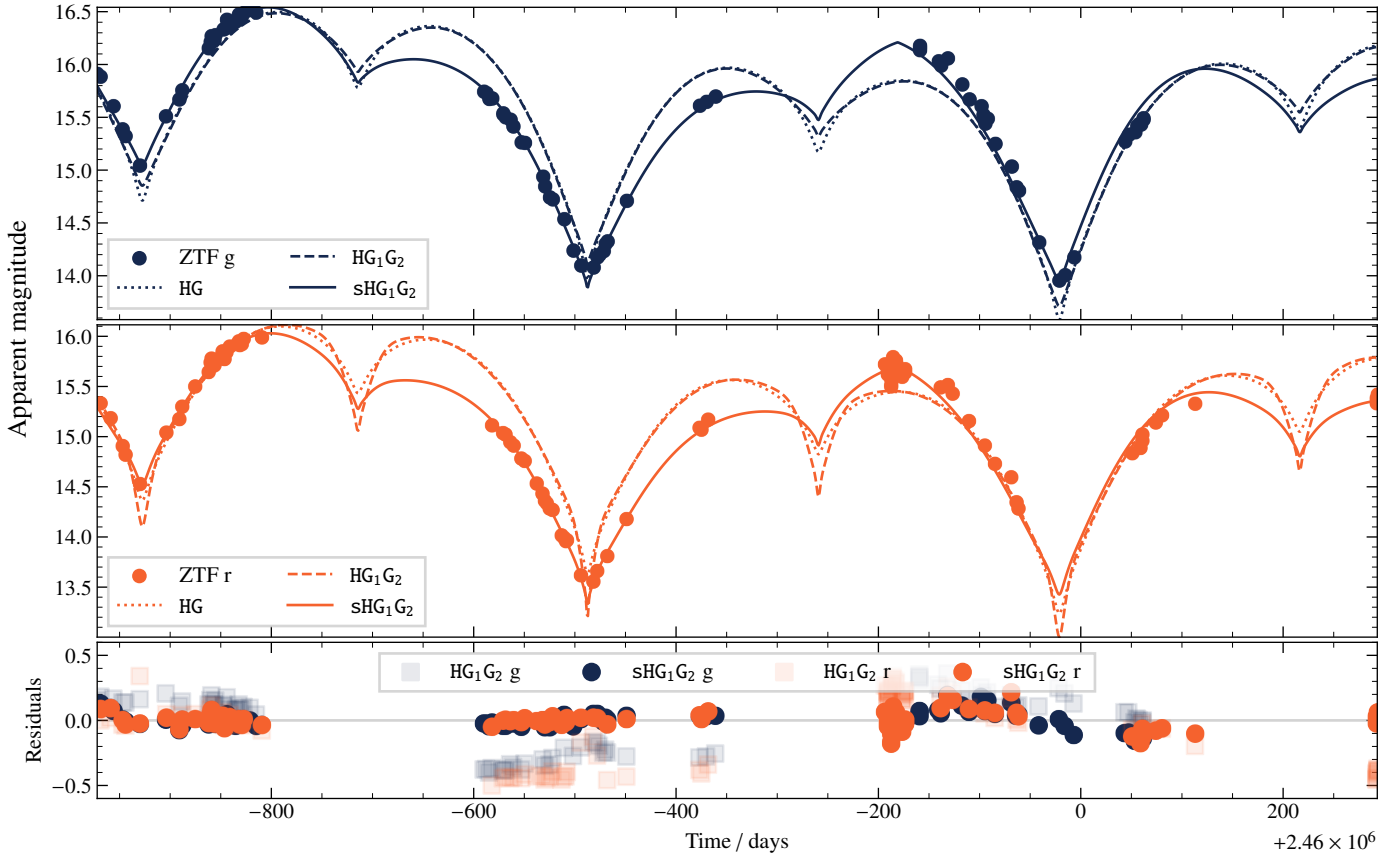

Fig. 3. Comparison of the HG, HG_1G_2, and sHG_1G_2 models on the photometry of (223) Rosa from ZTF.

observation with a Gaussian distribution within (a) the reported observational errors, and (b) ten times the reported observational errors. We again fit the models' parameters, and we restarted the procedure 500 times. In the (a) scenario, the results remain stable, within the reported standard deviations. On the contrary, the (b) scenario systematically leads to outlier values for the HG_1G_2 and sHG_1G_2 models, similar to what is observed in the initial dataset. Although this is perhaps not the only reason, we are confident that the rate of success should improve with higher signal-to-noise measurements, such as the data that will be soon collected by the *Vera C. Rubin* Observatory.

4.2. Fit to data

We compared the root-mean-square (RMS) residuals between the predicted photometry of the HG, HG_1G_2, and sHG_1G_2 models and the ZTF photometry in g and r in Fig. 4. The improvement of HG_1G_2 over HG (Fig. 4, left) is marginal, with all SSOs close to the diagonal. The improvement of sHG_1G_2 over HG_1G_2 (Fig. 4, right) is clear, and over HG (Fig. 4, middle) it is striking, with a significant tail below the diagonal.

The bulk of the population remains close to the diagonal. This implies that the predictions by HG or HG_1G_2 fit equally well the data as sHG_1G_2, although the latter has more degrees of freedom. There are three cases in which sHG_1G_2 may not be required. First, if the SSO is (nearly) spherical, its orientation will not significantly change its brightness. The $s(\alpha, \delta)$ term of sHG_1G_2 is therefore not required and converges toward zero. Second, if obliquity of the SSO is close to either 0° or 180° (as expected from YORP evolution, and as it is often the case, see Sect. 4.5 and Vokrouhlický et al. 2015; Ďurech et al. 2015; Ďurech & Hanuš 2023), as the orbital inclination is small the range of the aspect angle, Λ, covered remains limited around 90°. The brightness hence barely changes over apparitions, and the shape or spin term ($s(\alpha, \delta)$) contribution is minimal. Third, depending on the time span (mainly the number of apparitions) and number of observations, the range of the aspect angle, Λ, may again be limited. These three limiting cases are visible in Fig. 5.

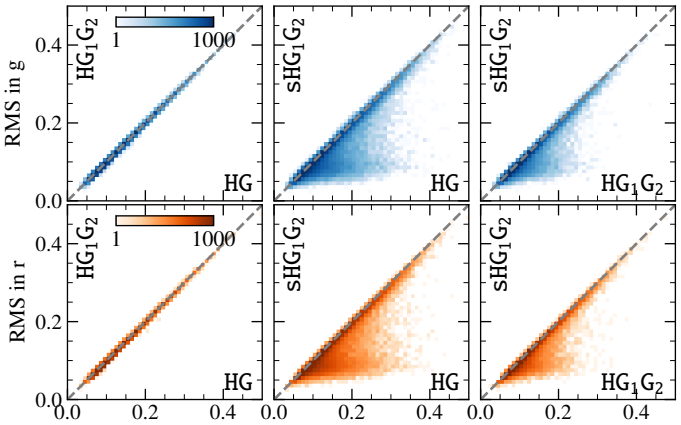

Fig. 4. Comparison of the residuals for the HG, HG_1G_2, and sHG_1G_2 models in both g and r filters.

Two conclusions can be drawn from this comparison of RMS. First, the sHG_1G_2 model indeed provides a clear improvement over the previous models. Second, this improvement is not always needed, for the reasons listed above. Pragmatically, this implies that the HG, HG_1G_2, and sHG_1G_2 models should be

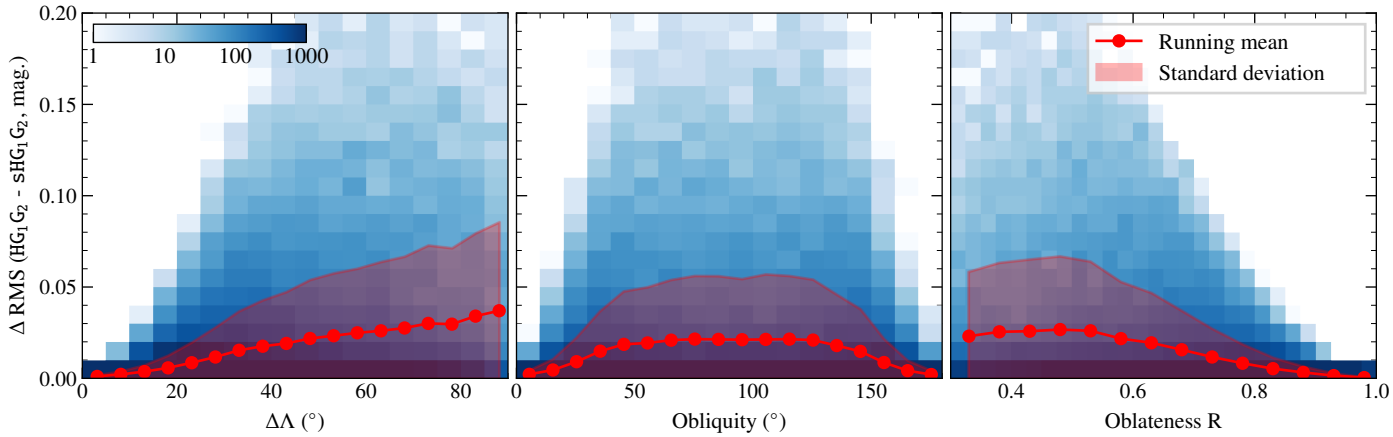

Fig. 5. Comparison of the residuals for the $\mathtt{HG_1G_2}$ and $\mathtt{sHG_1G_2}$ models as a function of the range of the aspect angle ($\Delta\Lambda$), the obliquity, and the oblateness, R. Larger values of ΔRMS indicate cases where $\mathtt{sHG_1G_2}$ improves over $\mathtt{HG_1G_2}$.

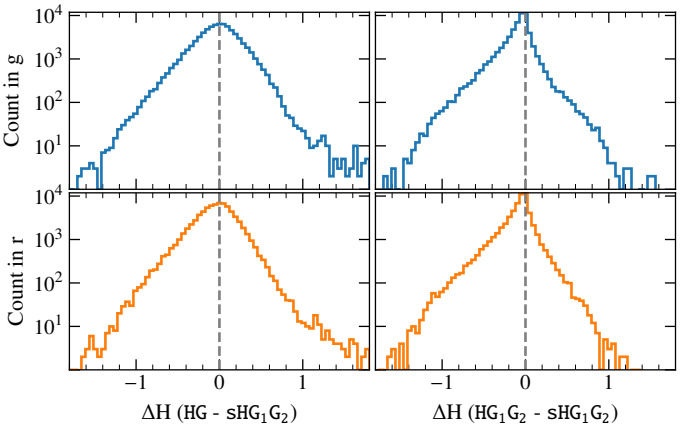

Fig. 6. Comparison of the absolute magnitude in $\mathtt{sHG_1G_2}$ with $\mathtt{HG}$ and $\mathtt{HG_1G_2}$, in the g and r filters.

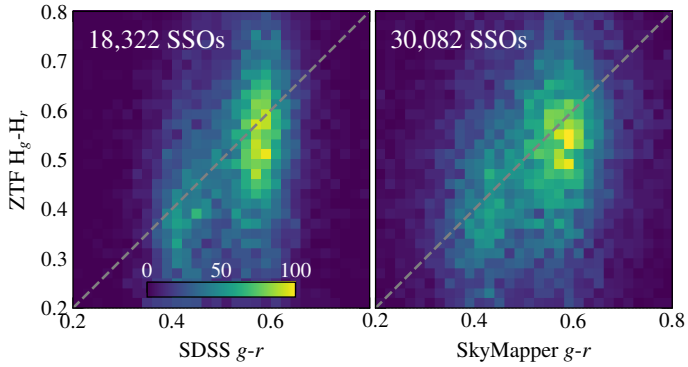

Fig. 7. g–r color from $\mathtt{sHG_1G_2}$ absolute magnitudes (H_g and H_r) compared with apparent SDSS and SkyMapper g–r colors (all converted to the PanSTARRS photometric system; see text).

computed for each SSO (in Fink but more generally at any ephemerides computation center): from the most robust to the most informative. In the pathological cases listed above, $\mathtt{HG_1G_2}$ should then be preferred over $\mathtt{sHG_1G_2}$. Similarly, if low phase angles are not covered, the two-parameter $\mathtt{G_1G_2}$ function, $g(\gamma)$ (common to $\mathtt{HG_1G_2}$ and $\mathtt{sHG_1G_2}$), is not constrained (see Mahlke et al. 2021) and $\mathtt{HG}$ should be preferred.

4.3. Absolute magnitude

We compare in Fig. 6 the $\mathtt{sHG_1G_2}$ absolute magnitude in g and r with those obtained with $\mathtt{HG}$ and $\mathtt{HG_1G_2}$. The three models are in good agreement, as is shown by the mode of 0 in their difference in absolute magnitude. The dispersion between $\mathtt{sHG_1G_2}$ and $\mathtt{HG_1G_2}$ is much smaller than with $\mathtt{HG}$, owing to the shared definition of the phase function, $g(\gamma)$, between the two models that differs from $\mathtt{HG}$. The two-parameter ($\mathtt{G_1G_2}$) function, $g(\gamma)$, was introduced by Muinonen et al. (2010) to better describe the opposition effect at small phase angles. It is therefore not unexpected to have differences in absolute magnitude between the two systems. There is a clear asymmetry in the absolute magnitude, as was expected from the definition of $\mathtt{sHG_1G_2}$ (Eq. (2)): the absolute magnitude is defined in the equatorial plane of the SSOs and is hence larger on average (the projection area on the plane of the sky is maximal for objects seen pole-on).

As an additional validation, we compare in Fig. 7 the ZTF g–r obtained from the H_g and H_r absolute magnitudes with the $\mathtt{sHG_1G_2}$ model and the g–r color from the SDSS and SkyMapper surveys (Sergeyev & Carry 2021; Sergeyev et al. 2022). The g and r of the three facilities differ, and the colors must therefore be corrected before any comparison. We converted all three systems to the PanSTARRS g–r color, using the following transformations: SkyMapper to SDSS (Sergeyev et al. 2022), SDSS to PanSTARRS (Finkbeiner et al. 2016), and ZTF to PanSTARRS (Medford et al. 2020). The distributions show a general trend toward the 1:1 relation, as was expected. The spread of values is larger for ZTF than for SDSS and SkyMapper, due to the fact that the ZTF magnitudes have an added uncertainty due to the computation via the phase curve, while SDSS and SkyMapper can compute the colors directly from the near-simultaneously acquired photometry. Two separate regions of higher density are visible, corresponding to the C and S taxonomy complexes (centered on g–r values of 0.4 and 0.55, respectively). This validates the approach of color determination from absolute magnitudes with the $\mathtt{sHG_1G_2}$ model.

4.4. Phase parameters $\mathtt{G_1G_2}$

We compare in Fig. 8 the values of $\mathtt{G_1G_2}$ obtained with the $\mathtt{sHG_1G_2}$ model with those from the $\mathtt{HG_1G_2}$ model. Both $\mathtt{G_1}$ and $\mathtt{G_2}$ show a good agreement, albeit some spread is present. The addition of the geometry term, $s(\alpha, \delta)$, in the definition of the

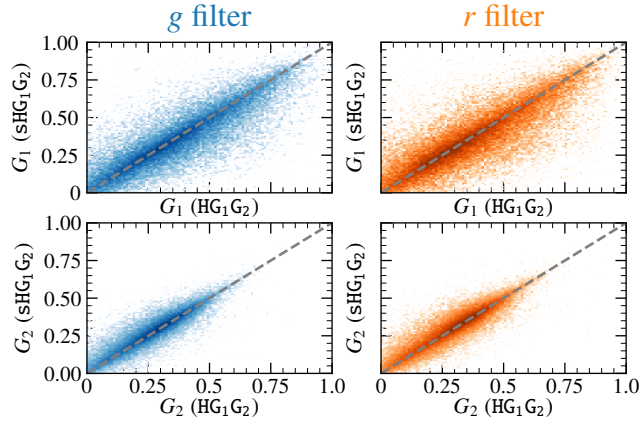

Fig. 8. Comparison of the G_1G_2 parameters in the g and r filters for the HG_1G_2 (x-axis) and sHG_1G_2 (y-axis) models.

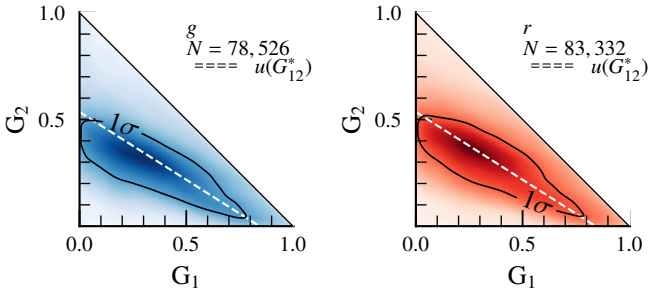

Fig. 9. Distribution of G_1G_2 parameters in g and r for the sHG_1G_2 model.

absolute magnitude (Eq. (2)) thus does not bias the slope parameters, G_1G_2. We further tested the values of these parameters in Fig. 9. For both the g and r filters, the bulk of the SSOs follow the $HG^{\star}_{12}$ line in the $\{G_1, G_2\}$ space (Muinonen et al. 2010; Penttilä et al. 2016; Shevchenko et al. 2016), again confirming the validity of the sHG_1G_2 model.

4.5. Spin coordinates

We compared the spin-axis coordinates (α_0,δ_0) derived with sHG_1G_2 and those available in the literature. We collected available spin solutions for the 95 593 SSOs in the FINK sample using the `SsODNet` service (Berthier et al. 2023). We find 6499 SSOs with previous estimates of the spin-axis coordinates, mainly from the light curve inversion technique (Kaasalainen et al. 2001) or in combination with other techniques (stellar occultations, direct imaging, and thermophysical modeling, Carry et al. 2010; Kaasalainen 2011; Ďurech et al. 2011; Viikinkoski et al. 2015; Hanuš et al. 2018a) by many authors (e.g., Hanuš et al. 2013a; Marciniak et al. 2021; Vernazza et al. 2021; Hung et al. 2022), compiled on the DAMIT[11] service (Ďurech et al. 2010).

We present in Fig. 10 the distribution of angular separation between the spin-axis coordinates from the literature and sHG_1G_2. The distribution peaks around 20°, with half of the SSOs agreeing below 35°. This is an overall good agreement, especially considering the limited number of observations available to the sHG_1G_2 model (92^{+46}_{-26}; see Sect. 3). We also present this distribution normalized by the spin uncertainty (computed as the quadratic sum of the uncertainties from the sHG_1G_2 and literature spin coordinates). About 60% of the solutions agree

[11] https://astro.troja.mff.cuni.cz/projects/damit/

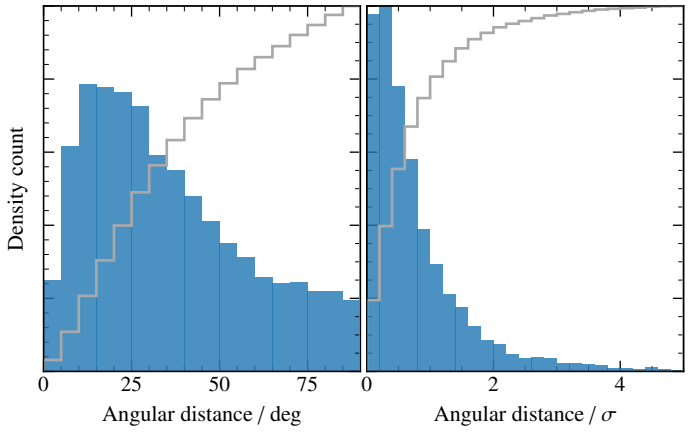

Fig. 10. Angular distance between spin-axis coordinates from sHG_1G_2 and the literature for 6499 asteroids, in degrees (left) and normalized by uncertainty (right). The cumulative distributions up to 100% are also presented (in gray).

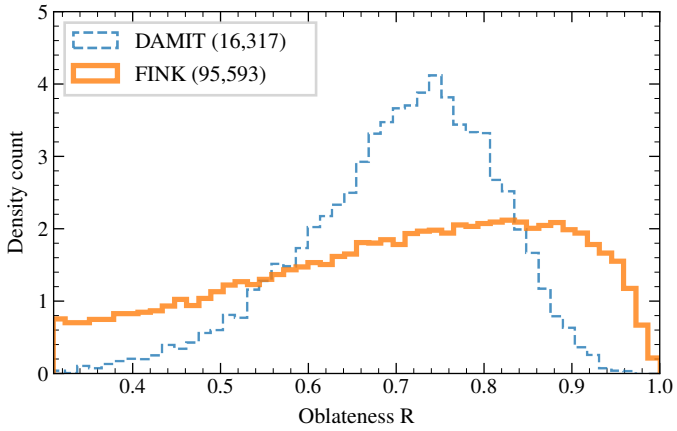

Fig. 11. Distribution of the oblateness, R, compared with that of 16 317 shape models of 10 743 asteroids from DAMIT (Ďurech et al. 2010).

within one σ, and 95% at three σ, an indication that the uncertainties seem to have been properly estimated (and not over- or underestimated).

4.6. Polar oblateness

We present the distribution of the polar oblateness, R, in Fig. 11, compared with that of existing 3D shape models from the literature. For that, we downloaded the 16 317 models of 10 743 unique asteroids available on DAMIT (Ďurech et al. 2010). These models are the product of inversion techniques (mainly Kaasalainen & Torppa 2001; Kaasalainen et al. 2001; Carry et al. 2010; Viikinkoski et al. 2015) from many authors (e.g., Ďurech et al. 2016, 2018; Hanuš et al. 2018b, 2021; Viikinkoski et al. 2017). We computed the oblateness, R, of all these models from Eq. (8), computing first the tri-axial diameters ($a \geq b \geq c$) from the moments of inertia (using the formulae by Dobrovolskis 1996).

The distribution of oblateness determined here presents two main differences with the one from the 3D shape models: it peaks at rounder objects (R of 0.9 rather than 0.7) and has a long tail toward flying saucers (low R). The tail is an artifact, as most SSOs with an oblateness below 0.5 have observations covering a very limited range of aspect angles and/or an obliquity close to

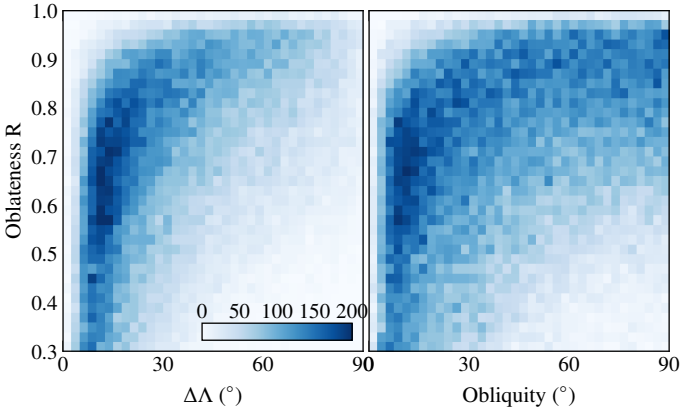

Fig. 12. Oblateness, R, as a function of the range of covered aspect angles ($\Delta\Lambda$) and obliquity (given the symmetry of $s(\alpha, \delta)$, we only plot obliquity in 0–90°).

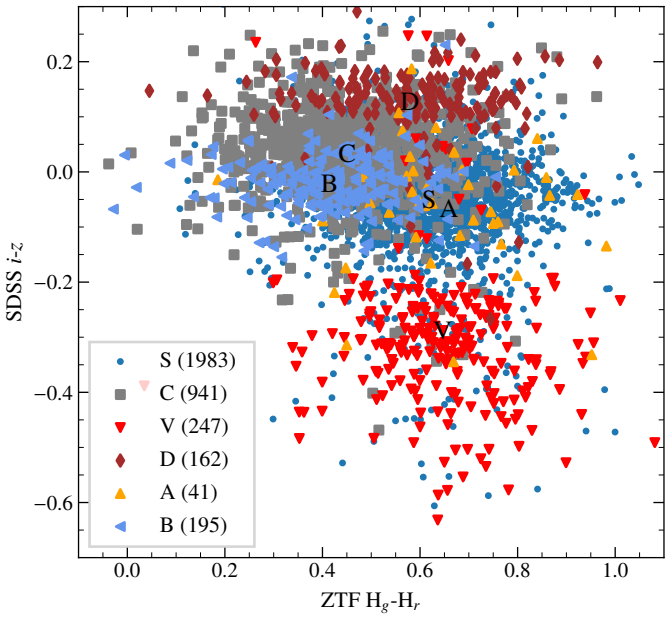

Fig. 13. Distribution of 3569 SSOs in SDSS i–z against ZTF H_g–H_r. The symbols and colors correspond to the taxonomic class retrieved from `SsODNet` (Berthier et al. 2023), and the letter mark the average color for each class.

either 0° or 180°, limiting the viewing geometry, as is shown in Fig. 12.

The shift in the center of the distribution is more complex to interpret and could be real or artificial. While the range of absolute magnitude between the FINK sample and the shape models from DAMIT overlap, the median absolute magnitude is 14.8 against 13.6. The SSOs reported here thus have a smaller diameter (with half typically smaller than 4 km). The distribution of oblateness between the two samples could genuinely be different. On the other hand, the difference aligns with intrinsic biases of both methods at play. As is shown by Marciniak et al. (2018), there is a clear bias against slow rotations and low-amplitude light curves among asteroids with a determined spin axis and 3D shape, even more marked as objects get fainter. The light curve inversion indeed favors targets with a strong intrinsic variability, which creates a bias against round asteroids (as $a > b > c$, large a/b ratios imply smaller R). This is confirmed, as asteroids with a 3D shape model generally have larger residuals with $\mathtt{sHG_1G_2}$ in ZTF data. Therefore, the distribution of oblateness for well-constrained solutions (e.g., large-enough $\Delta\Lambda$, valid $\mathtt{G_1G_2}$, low residuals) is likely representative of the real distribution of oblateness among asteroids. We plan to combine several datasets from different facilities, such as ZTF, ATLAS, PANSTARRS, *Gaia*, and LSST, to increase the time coverage, and hence the range of the observed aspect angle, Λ, to further constrain the obliquity and oblateness distributions.

5. Results

One of the main motivation to develop $\mathtt{sHG_1G_2}$ was the determination of reliable colors from sparse photometry of SSOs, such as that provided by the LSST. We show in Sect. 4.3 the validity of the approach. The dataset we use here (ZTF) only contains two filters (g and r) but it is enough as a proof of concept. We further illustrate the approach in Fig. 13, comparing ZTF H_g–H_r with SDSS i–z, mimicking the situation for LSST observations with absolute magnitudes determined with $\mathtt{sHG_1G_2}$ in all six LSST filters: u, g, r, i, z, and y (LSST Collaboration 2009). The different taxonomic groups are easily identified, and follow their expected location in such a "slope" (H_g–H_r) versus "one micron band" (i–z) plane (Ivezić et al. 2001; Nesvorný et al. 2005; DeMeo et al. 2009; DeMeo & Carry 2013; Sergeyev et al. 2023).

This is extremely promising for LSST: the $\mathtt{G_1G_2}$ of the phase function are better constrained with larger phase coverage (Mahlke et al. 2021), and as a result the absolute magnitude, H, is too. Furthermore, the longer the time spanned by the observation, the more geometries observed and the better the constraints on the spin axis and polar oblateness. With a factor of four to five times as many observations (400 vs 92^{+46}_{-26}) over a time interval three times longer (10 yr vs three), the colors obtained with the LSST will be much more precise (not to mention having a better intrinsic photometric accuracy).

We then present in Fig. 14 the distribution of the $\mathtt{G_1G_2}$ parameters for the g and r filters separately, for asteroids in the taxonomic complexes A, B, C, Ch, D, E, K, L, M, P, Q, S, V, and X (i.e., spectrally similar to E/M/P without albedo information), following the work by Mahlke et al. (2021). There is a clear trend in $\mathtt{G_1G_2}$ from low-albedo asteroids (C/P/D) occupying the high-$\mathtt{G_1}$-low-$\mathtt{G_2}$ region to the high-albedo asteroids (V/A/E) located toward low-$\mathtt{G_1}$-high-$\mathtt{G_2}$, as was expected (Shevchenko et al. 2016). The dispersion of each taxonomic group in Fig. 14 is more limited here than in Mahlke et al. (2021): this may be due to an intrinsically higher precision in ZTF photometry or the $\mathtt{sHG_1G_2}$ model being more adapted, or both. In any case, the strong correlation of $\mathtt{G_1G_2}$ with taxonomy opens up the possibility of using these parameters in the determination of asteroid taxonomic classes, especially with LSST photometry.

We compare the obliquity (computed from the spin coordinates determined with $\mathtt{sHG_1G_2}$) with the diameter (retrieved from `SsODNet`, Berthier et al. 2023) in Fig. 15. Asteroids larger than 50 km appear roughly isotropic (although an excess of direct rotators has been observed, Johansen & Lacerda 2010; Visser et al. 2020). Asteroids smaller than 10–20 km cluster toward extreme values of 0° and 180°, although there are many asteroids with an intermediate obliquity. This is a clear demonstration of the Yarkovsky–O'Keefe–Radzievskii–Paddack effect (Radzievskii 1952; Paddack 1969; O'Keefe 1976), or YORP for short (Vokrouhlický et al. 2015). This obliquity-diameter distribution has been known for years (e.g., Hanuš et al. 2013a; Ďurech et al. 2015) The sample of 95 593 from ZTF/$\mathtt{sHG_1G_2}$,

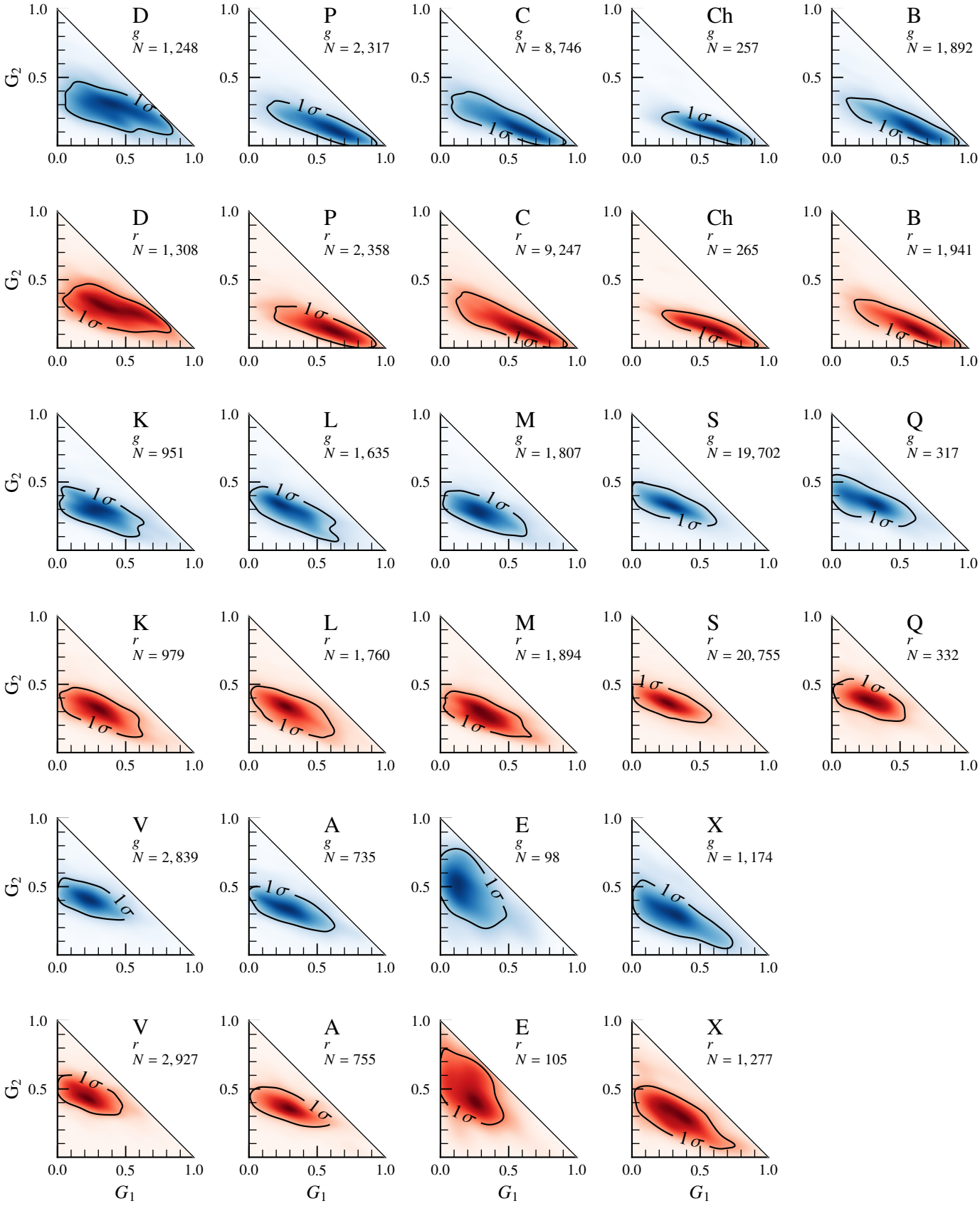

Fig. 14. Distribution of G_1G_2 parameters in *g* and *r* per taxonomic complex.

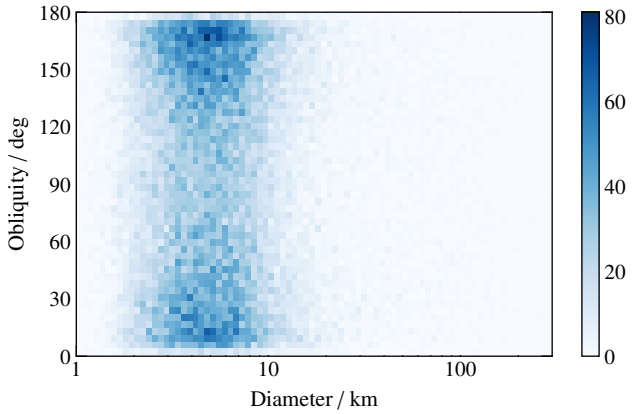

Fig. 15. Obliquity as a function of the diameter.

however, increases the sample of known obliquity by a factor of about ten.

The next logical step would be to study the distribution of obliquities among asteroids belonging to families, as was recently done by Ďurech & Hanuš (2023). However, the $\mathtt{sHG_1G_2}$ model is by construction symmetric across the equator of the target asteroid, and the determination of the spin-axis is thus ambiguous: the rotation can be either direct or retrograde. We hence report two spin solutions for each object in FINK: (α_0,δ_0) and (α_0+180,-δ_0).

We also study the distribution of ecliptic longitude of the pole. There is a strong correlation with the longitude of the ascending node, as was expected from a majority of SSOs with an obliquity close to either 0° or 180°: the longitude should be close to the longitude of the node minus 90°. We do not find a dependence between the distribution of longitude of the pole and the orbital inclination (Fig. 16), as opposed to Cibulková et al. (2016), who reported a more isotropic distribution of longitude for more inclined orbits. We compare the cumulative distributions of longitude for each range of inclination in Fig. 16. They are barely distinguishable from one another, which is confirmed by a Kolmogorov–Smirnov test: all the distributions are statistically similar.

6. Data availability

As was mentioned in Sect. 3, the data and results presented in the present study were all acquired and processed within FINK. The amount of SSOs for which a solution is determined, and the values of the parameters of the $\mathtt{sHG_1G_2}$ model, are therefore in constant evolution. FINK processes the incoming stream of alerts from ZTF on a daily basis, and the SSO parameters are determined once a month. The data and derived parameters reported here correspond to the SSOFT of December 2023.

As an official community broker of alerts for LSST, FINK will receive in real time the flow of alerts from the *Vera C. Rubin* Observatory. As such, the absolute magnitude, H, and $\mathtt{G_1G_2}$ in each of LSST filters, together with spin coordinates (α_0, δ_0) and polar oblateness (R), will be regularly determined and openly accessible to the scientific community for every SSO observed in the LSST.

The data and parameters can be retrieved from FINK Science Portal and API, in particular the summary table SSOFT containing all of the parameters. In the Python programming language, the data can be retrieved as follows[12]:

```
import requests

r = requests.post(
  "https://fink-portal.org/api/v1/ssoft",
  json={
    "flavor": "SHG1G2",
    "version": "2023.12",
    "output-format": "json"
  }
)
```

7. Conclusion

We propose a simple modification of the currently accepted $\mathtt{HG_1G_2}$ model to properly render the photometric behavior of SSOs taken over long periods of time. From observations in N_f filters, the new $\mathtt{sHG_1G_2}$ model simultaneously determines the absolute magnitude, H, and phase function coefficient, $\mathtt{G_1G_2}$, in each filter, the spin coordinates (α_0,δ_0), and the polar oblateness, R, for a total of $3 \times (N_f + 1)$ parameters. The determination of the absolute magnitude across multiple filters is required to determine the colors of SSOs in large sky surveys without back-to-back observations in different filters, such as the upcoming LSST of the *Vera C. Rubin* Observatory.

We tested the new $\mathtt{sHG_1G_2}$ model on observations in g and r, collected over 3 yr by the ZTF. The $\mathtt{sHG_1G_2}$ model provides a better description of the photometry, as is revealed by smaller residuals, than previous proposed models (HG and $\mathtt{HG_1G_2}$). The parameters determined by $\mathtt{sHG_1G_2}$ are nevertheless consistent with previous estimates. The absolute magnitude and phase parameters are in agreement with those determined with the $\mathtt{HG_1G_2}$ model on the same dataset, and the spin coordinates agree with those determined with other methods on different datasets within typically 20–30°. The polar oblateness presents a spurious trend toward small values, and a systematic shift in its peak value compared to SSOs with the shape model, which could be genuine but is also aligned with the expected biases of the different methods at play.

The limitations of the $\mathtt{sHG_1G_2}$ model are linked with the geometry of observations. Observations at a low phase angle (between 0° and 5°) are required to properly describe the opposition effect (affecting the $\mathtt{G_1G_2}$ parameters), a limitation inherited from the $\mathtt{HG_1G_2}$ model. The spin orientation and oblateness cannot be properly retrieved from observations spanning only a limited range of geometries, in particular the aspect angle. Finally, by construction of the model, there is a complete degeneracy between direct and retrograde rotation. The new term, $s(\alpha, \delta)$, accounting for the oblateness and orientation can, however, also be introduced in the HG and sHG models. Practically, all four models – HG, sHG, $\mathtt{HG_1G_2}$, and $\mathtt{sHG_1G_2}$ – should be computed for each SSO. Then, following the principle of Occam's razor, the simplest model, among those fitting the data satisfactorily, should be chosen and used.

The $\mathtt{sHG_1G_2}$ model is fully implemented in FINK, a broker of alerts for the LSST. The results of the model are freely available on the FINK portal for all of the SSOs observed by ZTF – and

[12] More information at https://fink-portal.org/api

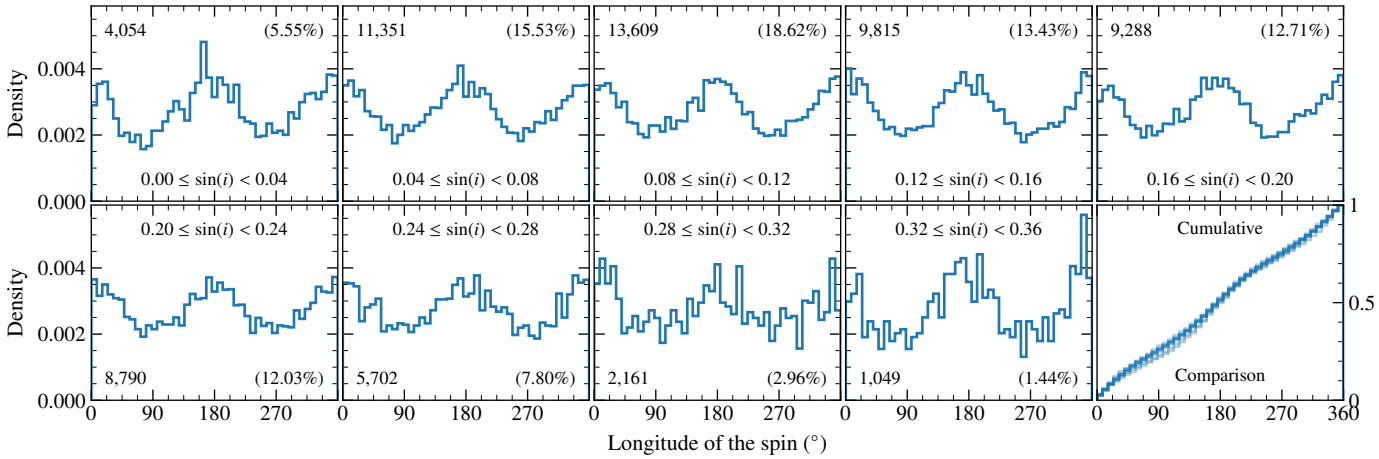

Fig. 16. Distribution of the ecliptic longitude of the spin axis as a function of the orbital inclination.

by the LSST in the near future – for which the fitting procedure has been successful.

Acknowledgements. This project has received financial support from the CNRS through the MITI interdisciplinary program. B.C. was supported by CNRS/INSU/PNP. We thank these programs for their support. This research used the `Miriade` (Berthier et al. 2009), `SsODNet` (Berthier et al. 2023), and `TOPCAT` (Taylor 2005) Virtual Observatory tools. It used the `astropy` (Astropy Collaboration 2013, 2018, 2022), `sbpy` (Mommert et al. 2019), and `rocks` (Berthier et al. 2023) python packages. This work was developed within the FINK community and made use of the FINK community broker resources. FINK is supported by LSST-France and CNRS/IN2P3. Thanks to all the developers and maintainers.

References

Agostini, L., Lucchetti, A., Pajola, M., et al. 2022, Planet. Space Sci., 216, 105476
Aivazyan, V., Almualla, M., Antier, S., et al. 2022, MNRAS, 515, 6007
Alvarez-Candal, A. 2024, A&A, 685, A29
Alvarez-Candal, A., Jimenez Corral, S., & Colazo, M. 2022, A&A, 667, A81
Astropy Collaboration (Robitaille, T. P., et al.) 2013, A&A, 558, A33
Astropy Collaboration (Price-Whelan, A. M., et al.) 2018, AJ, 156, 123
Astropy Collaboration (Price-Whelan, A. M., et al.) 2022, ApJ, 935, 167
Bellm, E. C., Kulkarni, S. R., Graham, M. J., et al. 2019, PASP, 131, 018002
Berthier, J., Hestroffer, D., Carry, B., et al. 2009, in Eur. Planet. Sci. Congress 2009, 676
Berthier, J., Carry, B., Vachier, F., Eggl, S., & Santerne, A. 2016, MNRAS, 458, 3394
Berthier, J., Carry, B., Mahlke, M., & Normand, J. 2023, A&A, 671, A151
Binzel, R. P., DeMeo, F. E., Turtelboom, E. V., et al. 2019, Icarus, 324, 41
Bottke, W. F., Vokrouhlický, D., Broz, M., Nesvorný, D., & Morbidelli, A. 2001, Science, 294, 1693
Bowell, E., Hapke, B., Domingue, D., et al. 1989, Asteroids II, 524
Bus, S. J., & Binzel, R. P. 2002, Icarus, 158, 146
Carry, B. 2018, A&A, 609, A113
Carry, B., Dumas, C., Kaasalainen, M., et al. 2010, Icarus, 205, 460
Carry, B., Solano, E., Eggl, S., & DeMeo, F. 2016, Icarus, 268, 340
Carvano, J. M., & Davalos, J. A. G. 2015, A&A, 580, A98
Chang, C.-K., Ip, W.-H., Lin, H.-W., et al. 2015, ApJ, 219, 27
Cibulková, H., Ďurech, J., Vokrouhlický, D., Kaasalainen, M., & Oszkiewicz, D. A. 2016, A&A, 596, A57
Colazo, M., Duffard, R., & Weidmann, W. 2021, MNRAS, 504, 761
De Prá, M. N., Pinilla-Alonso, N., Carvano, J. M., et al. 2018, Icarus, 311, 35
DeMeo, F. E., & Carry, B. 2013, Icarus, 226, 723
DeMeo, F. E., & Carry, B. 2014, Nature, 505, 629
DeMeo, F., Binzel, R. P., Slivan, S. M., & Bus, S. J. 2009, Icarus, 202, 160
DeMeo, F. E., Binzel, R. P., Carry, B., Polishook, D., & Moskovitz, N. A. 2014, Icarus, 229, 392
Devogèle, M., Tanga, P., Cellino, A., et al. 2018, Icarus, 304, 31
Dobrovolskis, A. R. 1996, Icarus, 124, 698
Ďurech, J., & Hanuš, J. 2018, A&A, 620, A91
Ďurech, J., & Hanuš, J. 2023, A&A, 675, A24
Ďurech, J., Hanuš, J., Oszkiewicz, D., & Vančo, R. 2016, A&A, 587, A48
Ďurech, J., Hanuš, J., & Alí-Lagoa, V. 2018, A&A, 617, A57
Ďurech, J., Hanuš, J., & Vančo, R. 2019, A&A, 631, A2
Ďurech, J., Kaasalainen, M., Marciniak, A., et al. 2007, A&A, 465, 331
Ďurech, J., Sidorin, V., & Kaasalainen, M. 2010, A&A, 513, A46
Ďurech, J., Kaasalainen, M., Herald, D., et al. 2011, Icarus, 214, 652
Ďurech, J., Carry, B., Delbo, M., Kaasalainen, M., & Viikinkoski, M. 2015, Asteroid Models from Multiple Data Sources (University of Arizona Press), 183
Farinella, P., Vokrouhlický, D., & Hartmann, W. K. 1998, Icarus, 132, 378
Ferrais, M., Jorda, L., Vernazza, P., et al. 2022, A&A, 662, A71
Finkbeiner, D. P., Schlafly, E. F., Schlegel, D. J., et al. 2016, ApJ, 822, 66
Galinier, M., Delbo, M., Avdellidou, C., Galluccio, L., & Marrocchi, Y. 2023, A&A, 671, A40
Galluccio, L., Delbo, M., De Angeli, F., et al. 2023, A&A, 674, A35
Graham, M. J., Kulkarni, S. R., Bellm, E. C., et al. 2019, PASP, 131, 078001
Grasset, O., Dougherty, M. K., Coustenis, A., et al. 2013, Planet. Space Sci., 78, 1
Hanuš, J., Ďurech, J., Brož, M., et al. 2013a, A&A, 551, A67
Hanuš, J., Brož, M., Durech, J., et al. 2013b, A&A, 559, A134
Hanuš, J., Delbo, M., Ďurech, J., & Alí-Lagoa, V. 2018a, Icarus, 309, 297
Hanuš, J., Delbo, M., Alí-Lagoa, V., et al. 2018b, Icarus, 299, 84
Hanuš, J., Pejcha, O., Shappee, B. J., et al. 2021, A&A, 654, A48
Hung, D., Hanuš, J., Masiero, J. R., & Tholen, D. J. 2022, PSJ, 3, 56
IMCCE 2021, Introduction aux éphémérides et phénomènes astronomiques, eds. J. Berthier, P. Descamps, & F. Mignard (EDP Sciences)
Ivezić, Ž., Tabachnik, S., Rafikov, R., et al. 2001, AJ, 122, 2749
Jackson, S. L., Rozitis, B., Dover, L. R., et al. 2022, MNRAS, 513, 3076
Johansen, A., & Lacerda, P. 2010, MNRAS, 404, 475
Jones, R. L., Chesley, S. R., Connolly, A. J., et al. 2009, Earth Moon Planets, 105, 101
Kaasalainen, M. 2004, A&A, 422, L39
Kaasalainen, M. 2011, Inverse Probl. Imaging, 5, 37
Kaasalainen, M., & Torppa, J. 2001, Icarus, 153, 24
Kaasalainen, M., Torppa, J., & Muinonen, K. 2001, Icarus, 153, 37
Kaasalainen, M., Torppa, J., & Piironen, J. 2002, Icarus, 159, 369
Kalup, C. E., Molnár, L., Kiss, C., et al. 2021, ApJS, 254, 7
Kwiatkowski, T., & Kryszczynska, A. 1992, in Liege International Astrophysical Colloquia, 30, eds. A. Brahic, J. C. Gerard, & J. Surdej, 353
Lazzaro, D., Angeli, C. A., Carvano, J. M., et al. 2004, Icarus, 172, 179
Le Montagner, R., Peloton, J., Carry, B., et al. 2023, A&A, 680, A17
Leoni, M., Ishida, E. E. O., Peloton, J., & Möller, A. 2022, A&A, 663, A13
LSST Collaboration (Abell, P. A., et al.) 2009, arXiv e-prints [arXiv:0912.0201]
Lucas, M. P., Emery, J. P., Pinilla-Alonso, N., Lindsay, S. S., & Lorenzi, V. 2017, Icarus, 291, 268
Mahlke, M., Carry, B., & Denneau, L. 2021, Icarus, 354, 114094
Mahlke, M., Carry, B., & Mattei, P. A. 2022, A&A, 665, A26
Marciniak, A., Bartczak, P., Müller, T., et al. 2018, A&A, 610, A7
Marciniak, A., Ďurech, J., Alí-Lagoa, V., et al. 2021, A&A, 654, A87
Martikainen, J., Muinonen, K., Penttilä, A., Cellino, A., & Wang, X. B. 2021, A&A, 649, A98
Masci, F. J., Laher, R. R., Rusholme, B., et al. 2019, PASP, 131, 018003
Medford, M. S., Lu, J. R., & Schlafly, E. F. 2020, RNAAS, 4, 38
Möller, A., Peloton, J., Ishida, E. E. O., et al. 2021, MNRAS, 501, 3272

Mommert, M., Kelley, M., de Val-Borro, M., et al. 2019, J. Open Source Softw., 4, 1426
Muinonen, K., Belskaya, I. N., Cellino, A., et al. 2010, Icarus, 209, 542
Muinonen, K., Torppa, J., Wang, X. B., Cellino, A., & Penttilä, A. 2020, A&A, 642, A138
Nesvorný, D., Jedicke, R., Whiteley, R. J., & Ivezić, Ž. 2005, Icarus, 173, 132
O'Keefe, J. A. 1976, Tektites and their origin (NASA Goddard Space Flight Center)
Ostro, S. J., Margot, J.-L., Benner, L. A. M., et al. 2006, Science, 314, 1276
Oszkiewicz, D. A., Muinonen, K., Bowell, E., et al. 2011, JQSRT, 112, 1919
Oszkiewicz, D., Klimczak, H., Carry, B., et al. 2023, MNRAS, 519, 2917
Paddack, S. J. 1969, J. Geophys. Res., 74, 4379
Pajuelo, M., Carry, B., Vachier, F., et al. 2018, Icarus, 309, 134
Pál, A., Szakáts, R., Kiss, C., et al. 2020, ApJS, 247, 26
Patterson, M. T., Bellm, E. C., Rusholme, B., et al. 2019, PASP, 131, 018001
Penttilä, A., Shevchenko, V. G., Wilkman, O., & Muinonen, K. 2016, Planet. Space Sci., 123, 117
Popescu, M., Licandro, J., Morate, D., et al. 2016, A&A, 591, A115
Popescu, M., Licandro, J., Carvano, J. M., et al. 2018, A&A, 617, A12
Radzievskii, V. V. 1952, AZh, 29, 162
Rodrigo, C., Solano, E., & Bayo, A. 2012, SVO Filter Profile Service Version 1.0, IVOA Working Draft 15 October 2012
Sanchez, J. A., Reddy, V., Nathues, A., et al. 2012, Icarus, 220, 36
Seares, F. H. 1930, PASP, 42, 5
Sergeyev, A. V., & Carry, B. 2021, A&A, 652, A59
Sergeyev, A. V., Carry, B., Onken, C. A., et al. 2022, A&A, 658, A109
Sergeyev, A. V., Carry, B., Marsset, M., et al. 2023, A&A, 679, A148
Shevchenko, V. G., Belskaya, I. N., Muinonen, K., et al. 2016, Planet. Space Sci., 123, 101
Shevchenko, V. G., Belskaya, I. N., Mikhalchenko, O. I., et al. 2019, A&A, 626, A87
Shevchenko, V. G., Mikhalchenko, O. I., Belskaya, I. N., et al. 2021, Planet. Space Sci., 202, 105248
Shevchenko, V. G., Belskaya, I. N., Slyusarev, I. G., et al. 2022, A&A, 666, A190
Sierks, H., Lamy, P., Barbieri, C., et al. 2011, Science, 334, 487
Slivan, S. M., Binzel, R. P., Crespo da Silva, L. D., et al. 2003, Icarus, 162, 285
Solano, E., Rodrigo, C., Pulido, R., & Carry, B. 2014, Astron. Nachr., 335, 142
Spoto, F., Tanga, P., Mignard, F., et al. 2018, A&A, 616, A13
Tanga, P., Carry, B., Colas, F., et al. 2015, MNRAS, 448, 3382
Taylor, M. B. 2005, in ASP Conf. Ser., 347, Astronomical Data Analysis Software and Systems XIV, eds. P. Shopbell, M. Britton, & R. Ebert, 29
Torppa, J., Kaasalainen, M., Michalowski, T., et al. 2003, Icarus, 164, 346
Vernazza, P., Ferrais, M., Jorda, L., et al. 2021, A&A, 654, A56
Veverka, J., Robinson, M., Thomas, P., et al. 2000, Science, 289, 2088
Viikinkoski, M., Kaasalainen, M., & Durech, J. 2015, A&A, 576, A8
Viikinkoski, M., Hanuš, J., Kaasalainen, M., Marchis, F., & Ďurech, J. 2017, A&A, 607, A117
Visser, R. G., Ormel, C. W., Dominik, C., & Ida, S. 2020, Icarus, 335, 113380
Vokrouhlický, D., Brož, M., Bottke, Jr., W. F., Nesvorný, D., & Morbidelli, A. 2006, Icarus, 182, 118
Vokrouhlický, D., Bottke, W. F., Chesley, S. R., Scheeres, D. J., & Statler, T. S. 2015, The Yarkovsky and YORP Effects, eds. P. Michel, F. DeMeo, & W. F. Bottke, 509
Waszczak, A., Chang, C.-K., Ofek, E. O., et al. 2015, AJ, 150, 75
Xu, S., Binzel, R. P., Burbine, T. H., & Bus, S. J. 1995, Icarus, 115, 1
Zellner, B., Tholen, D. J., & Tedesco, E. F. 1985, Icarus, 61, 355